Tryptophan Contributions to the Empirical Free-Energy Profile in Gramicidin A/M Heterodimer Channels

Jacob Devin Durrant, Devin Caywood, and David D. Busath
Deptartment of Physiology and Developmental Biology, Brigham Young University, Provo, Utah

ABSTRACT Gramicidin A/gramicidin M heterodimer conductances were measured in planar lipid bilayers and found to form two distinguishable populations about halfway between the gramicidin A and gramicidin M homodimer conductances. This implies that the principle difference in the gramicidin A and gramicidin M transport free-energy profiles occurs at the channel center, where it would produce similar effects on the rate-limiting barrier for the two heterodimers. Kinetic analysis based on this and nearly all previously published homodimer conductance data for both gramicidin A and gramicidin M channels confirms this conclusion, indicating that the translocation step is ~100-fold slower in gramicidin M homodimers than in gramicidin A homodimers and that first- and second-ion exit-rate constants are higher by factors of 24 and 10, respectively. Assuming that the ratios of rate constants are related to the free-energy difference between gramicidin A and gramicidin M, we construct an effective ion-Trp free-energy interaction profile that has a minimum at the channel center.

INTRODUCTION

Ion currents through molecular channels like gramicidin can readily be measured with >10% accuracy and precision (1–8), so changes in rate-limiting energy barriers as small as 0.1 *RT* can be detected experimentally. Empirical atomistic force fields for biomolecules, on the other hand, have implicit uncertainties on the order of *RT* with respect to, for example, such things as peptide hydration energies (9). This article describes how the results of gramicidin conductance measurements were used in conjunction with rate-theory analysis to obtain a gramicidin A (gA)/gramicidin M (gM) free-energy difference profile.

The gA channel is a head-to-head homodimer of linear pentadecapeptides composed of amino acids that alternate in effective chirality. The peptide forms a tightly twisted helical β-strand (10) that has a right-handed twist (11–13) and a central pore ~4.0 Å in diameter. Gramicidin channels are permeable to small monovalent cations, including H^+, Na^+, K^+, and Cs^+ (14). End-to-end gramicidin dimers are readily amenable to heterodimer studies (15,16), where one-half of the otherwise symmetrical channel, corresponding to the passageway through one monolayer leaflet in a lipid bilayer, is modified in sequence. Thus far, such studies have been used primarily to explore dimerization kinetics and energetics and have observed that heterodimers display kinetics intermediate between their component homodimers, suggesting that the monomer structures, lipid interactions, and dynamics are similar in homodimer and heterodimer constructs. We therefore assume that the monomer structures in the heterodimers are similar to those in the homodimers and that the electric field along the ion transport pathway will therefore be the superposition of the fields from each of the two monomers. Because the entry and exit are >10 Å from the center of the channel and near (<2.5 Å from) the ion-binding site, we also assume that ion entry and exit rates for each monomer of the heterodimer are the same as for their corresponding homodimer.

The primary natural variant, gA, has tryptophans at positions 9, 11, 13, and 15 near the channel entrance and exit. The tryptophan side chain has a significant dipole moment producing an electric field that projects into the channel lumen and influences channel conductance (8,17–23).

gM and its chiral invert, gM^-, are analogs of gA in which the four Trp residues are replaced with Phe residues, thus eliminating the Trp effects on the axial free-energy profile. Replacement of Trp side chains with nonpolar residues like Phe inhibits alkali cation current flow through gramicidin channels by nearly an order of magnitude (18,24–30).

The free-energy profiles for Na^+ and K^+ transport through the gA channel have been calculated using umbrella-sampling molecular dynamics simulations (31–33). The principle features of these profiles are a barrier-free entry well on each side of the channel separated by a large central barrier. With corrections for periodic boundary artifacts, bilayer dielectric properties, and effects related to high-bath concentrations, the one-dimensional free-energy surface used with the Nernst-Planck equation predicts currents within a factor of 0.02–0.04 of those measured, which is considered reasonably successful given the high sensitivity of conductance to the rate-limiting free-energy barrier height (33).

Previously, a coherent pattern was observed in the conductances of gA and gM channels embedded in lipid bilayers of implicitly differing and reagent-modulated interfacial dipole potentials, indicating that both Trp side chains and the interfacial dipole potential modulate the effective height of a high central barrier (30). These results complement prior

Submitted November 29, 2005, and accepted for publication June 19, 2006.

Jacob Devin Durrant and Devin Caywood contributed equally to the project.

Address reprint requests to David D. Busath, Dept. of Physiology and Developmental Biology, Brigham Young University, Provo, UT 84602. Tel.: 801-422-8753; Fax: 801-422-0700; E-mail: david_busath@byu.edu.

0006-3495/06/11/3230/12 $2.00

doi: 10.1529/biophysj.105.078782

speculations that the dominant Trp effect is ion stabilization at the center of the channel (19,24,34). The idea of quantifying dipole effects from side chains by examining the fit of rate theory models for closely related gramicidin variants was first explored with a single Trp-to-Phe mutant (28) with limited success.

Subsequently, rate-theory analysis of energy perturbations due to fluorination of Trp side chains culminated (8) in the conclusion that electrostatic predictions based on the CHARMM united atom (v. 19) force field were consistent with rate-theory fit observations for the four 5-fluorination (5-F) Trp analogs and for 6-F Trp-9 gA, but 6-F of Trps 11, 13, or 15 yielded opposite results, suggesting that fluorination at the more externally situated C6 site may lead to additional polarization by the lipid headgroups or bulk water. In the fluorination studies, the central barrier is reduced by the F-Trp side chains, and the central barrier loses its clear, rate-limiting status. Therefore, in this study we focus on perturbations that are expected to increase the central barrier.

Rate-theory modeling is appealing and successful with gramicidin single-channel current analysis for several reasons. The channels are single-file, cylindrical pores (11), with a simple reaction coordinate for ion transport. They have well established binding sites near each end of the channel, and very little occupancy in the middle of the channel, according to NMR and x-ray diffraction studies (35–37). At the highest membrane potentials attainable and with low ion concentrations in the bath, entry is clearly rate-limiting but has virtually no voltage dependence (5,38,39), implying that the path into the binding site is essentially barrier-free. (The first and third barriers in the three-barrier, two-site model can be considered a simple heuristic to represent the diffusive entry and the discrete-step exit processes). Finally, because the energy steps for exit and translocation are several kcal/mol, rate theory is as accurate as continuum theory (40) and probably more efficient for the modeling of large data sets.

At this stage, no information is available on the structural impact of mutating a gramicidin Trp to a Phe. The conformation of a Phe side chain might be expected to be less stable than that of Trp because of the featureless nature of the benzene ring. For simplicity, we assume in this article that the net electrostatic potential of the Phe side chain does not affect cation passage through the channel because it is nonpolar. We also assume that the Trp side chains have no impact on ion entry into the channel because of local shielding or on channel conformation. These assumptions will need to be explored more carefully with structural and simulation studies in the future.

Here we further test the Trp central barrier reduction hypothesis using heterodimer channels comprised of gA at one end and gM at the other. Initial experimental studies of these channels (29) were substantially augmented for the purpose of the rate-theory analysis applied here. These heterodimer channels have the influence of the Trp side chain on ion permeation from the four side chains on one end of the channel but not the other. For K^+ and Cs^+ transport, the fact that the ion stays near the axis during transport justifies our focus on the Trp side-chain potential on the channel axis. For measurements with Na^+, we assume that the average of the ion side-chain energy along the helical trajectory of the ion through the channel would be similar to the axial potential. We postulated that there would be a limited number of axial Trp free-energy profiles (hereafter referred to as Trp profiles) that could explain the currents observed for heterodimers oriented in opposite directions. Namely, if the central barrier alone were affected by the Trp profile, the orientation of the heterodimers should not matter much, whereas if the binding affinity on the gM side of the channel were primarily affected, the orientation should have a dramatic effect on channel conductance. Here we report that the consequences of orientation are small but measurable, and we utilize the result in the context of a global application of rate theory to nearly all of the gA conductance data available in the literature to assess the shape of the net Trp side-chain profile. In conjunction with earlier observations of extreme superlinearity in the gM current-voltage relationship (25), the results imply that the gM-gA free-energy difference profile is somewhat negative in the region of the binding sites and becomes much more negative at the center of the channel.

MATERIALS AND METHODS

Single heterodimer channel current measurements

Heterodimer channel experiments were performed under the conditions described previously (29). gA was obtained from ICN Pharmaceuticals (Cleveland, OH) and diluted in methanol to a concentration of $\sim 10^{-5}$ mg/ml. gM was prepared by solid-state synthesis using 9-fluorenylmethoxycarbonyl chemistry on an Applied Biosystems (Foster City, CA) model 430A peptide synthesizer and recrystallized after HPLC purification. Glycerylmonoolein (GMO) was obtained from NuChek Prep (Elysian, MN). Diphytanoylphosphatidylcholine (DPhPC) was obtained from Avanti Polar Lipids (Alabaster, AL). GMO was suspended in *n*-hexadecane at 50 mg/ml. DPhPC was mixed with *n*-decane at 20 mg/ml. Approximately 10–20 pg injections of peptide were added to 2–3 ml unbuffered KCl baths. The assignments of gA-gM and gM-gA peaks from these experiments were based on the results obtained with unilateral gA addition after bilayer formation in 1.0 M KCl in the presence of gM, which was expected to be randomly distributed in both leaflets. In this experiment, it was found that the heterodimer peak with the lower conductance represented the orientation in which the gM monomer was at the entrance and the gA monomer was at the exit. Due to the smoothness of the current concentration plots, it was assumed that this assignment applied at all concentrations.

Voltage (200 mV for DPhPC; 100 mV for GMO) was applied to the *trans* side of the membrane using Ag-AgCl electrodes, and single-channel currents were measured with a List Medical (Darmstadt, Germany) patch-clamp amplifier (BC-525C) using IGOR Pro software from Wave Metrics (Lake Oswego, OR). Analysis of channel current was performed using TAC and TACFit from Bruxton (Seattle, WA). Channels with signal-to-noise (channel conductance to peak-to-peak noise) ratios <1 were not analyzed. Experiments were performed at room temperature, 23°C. At least 50 channels were observed for each experiment, and three or more experiments were performed for each condition, the corresponding mean currents from the histogram peaks being averaged.

gA homodimer channel kinetic model parameterization

To lay the foundation for theoretical fits of the gA-gM heterodimer data, it was first necessary to solidify the kinetic parameter selection for gA homodimer conductance data. The parameters obtained from this effort are, at once, a synthesis of all previous measurements of factors related to gramicidin-channel conductance such as single-channel current-voltage-concentration relationships, binding affinity, binding-site localization, and molecular-dynamics simulations, thus serving as a foundation for future research.

The kinetics of gA were analyzed via the three-barrier, two-site, two-ion (3B2S) kinetic model, which accurately predicts the main conductance features of gA (8,23,28,30,41–43), in conjunction with the kinetic perturbation method described by Thompson et al. (23). Data sets for gA homodimer current-voltage-concentration relations were extracted from 11 publications (see Fig. 1 legend). Conversions to molal activities for bath concentrations were made using a piecewise-polynomial fit to published values. A database containing these and other gramicidin channel data are available in machine-readable text files at http://pdbio.byu.edu/faculty/db6/gramicidin.

Following the logic of Urban et al. (41), the two-site energy profile suggests that four mutually exclusive gramicidin channel states are possible, namely empty (00), left-hand occupied (10), right-hand occupied (01), and doubly occupied (11) where left and right correspond to the *cis* and *trans* sides of the channel. Ten rate constants ($A'_0\ s^{-1}\ M^{-1}$, $B'_0\ s^{-1}$, $K'_0\ s^{-1}$, $D'_0\ s^{-1}\ M^{-1}$, $E'_0\ s^{-1}$, $A''_0\ s^{-1}\ M^{-1}$, $B''_0\ s^{-1}$, $K''_0\ s^{-1}$, $D''_0\ s^{-1}\ M^{-1\prime}$, $E''_0\ s^{-1}$) represent the possible transitions between these four states. Primed rate constants represent movements from the left to the right, and double-primed rate constants represent movements from the right to the left. Specifically, A' is the rate at which an ion moves from bulk water to the left binding site of an unoccupied channel, B' is the rate at which an ion leaves the right binding site of a singly-occupied channel for bulk water, K' is the rate at which an ion moves from the left binding site to the right binding site, D' is the rate at which an ion moves from bulk water to the left binding site of a right-site occupied channel, and E' is the rate at which an ion leaves the right binding site of a doubly occupied channel for bulk water. When no voltage is applied across the membrane, each primed rate constant equals its doubly primed equivalent, so the prime notation is dropped.

The voltage-dependency constants that account for the effects of a voltage gradient on the rate constants are α_1, α_2, α_3, α_4, and α_5. They represent the fractional electrical distance from bulk solution on the left to the peak of the first (left-most) barrier, to the first binding site, to the center of the translocation (central) barrier, to the distant (right-most) binding site, and to the distance barrier, respectively. The rate constants described above are modified (41) assuming a linear voltage drop. These voltage-dependency parameters were not constrained in the fit, except for requirements that $\alpha_2 < 0.5$, $\alpha_1 < \alpha_2$, and $\alpha_3 = 0.5$. Note that in symmetrical homodimer channels, $\alpha_1 = 1 - \alpha_5$, and $\alpha_2 = 1 - \alpha_4$. In asymmetrical heterodimer channels, however, these equalities are not required.

The kinetic perturbation (or coupling constant) method (8,23) was used to represent long-range energy differences due to the lipid (e.g., interfacial dipole potential differences for GMO and DPhPC), the peptide (e.g., side-chain potential differences for gA and gM), or the ion (e.g., hydration/dehydration energy differences for Na^+ and K^+). In this approach, rate constant modification factors represent the natural logarithm of energetic perturbations to the major barriers to ion passage with the expectation that long-range energy factors should be additive and independent. The approach is helpful in that it automatically preserves microscopic reversibility. Coupling constants for Cs^+ were included in the gA homodimer fit, but were more strongly constrained in combination with the gM fits, so only the latter estimates are presented.

In addition to the current-voltage-concentration data mentioned above, other relevant gA data were fit simultaneously, including the first- and second-ion binding affinities (44), maximum entry rates (39), and Na^+ flux ratio exponents of 1.0 at 0.1 mM and 1.0 mM from radioisotope tracer experiments (45). Also, to represent the observations of Cole et al. (8) in fitting fluorinated gA and the effectiveness of interfacial dipole potential agents as observed by Duffin et al. (30), the translocation-rate coupling constant for the transition from DPhPC → GMO was confined to be ~8.5. The first- and second-ion binding affinities, $K_1 = A/B$ and $K_2 = D/E$, were both expected to differ in the two lipids only slightly due to long-range lipid potential effects at the binding sites, probably with higher affinity in GMO bilayers because of the lower GMO interfacial dipole potential (see references cited in Duffin et al. (30)). To avoid large disparities for the two lipids, we weakly constrained the first- and second-ion binding affinities to be approximately the same in the two lipids, allowing differences by up to a factor of ~2. For this and the other constraints mentioned above, a penalty was added to χ^2 for deviations from the observed conditions, with weights adjusted to balance the discrepancies among the different types of measurements. Finally, the rate constant for second ion entry, D, is poorly constrained but similar to that for first-ion entry, A. For lack of compelling evidence to the contrary, we constrained the two to be equal in the gA (but not the later gM) fits to simplify parameter space.

A steepest-descent approach was used to minimize the χ^2 error (difference between experimental observation and kinetic-theory prediction squares) with uncertainty weights derived from the standard-deviation equation given in Thompson et al. (23),

$$W(pA) = 0.0143\bar{i}(pA) + 0.0026pA, \qquad (1)$$

where $\bar{i}$ is the time-averaged single-channel current. These weights are used as approximations for the uncertainties from all labs, as standard deviations are often not provided in the literature. They produce rather strict estimates for a global fit because the equation is based on the optimal precision obtained in the Busath lab. Although there is good reproducibility between labs when identical conditions are compared (see below), Eq. 1 produces somewhat too high a value for the weighted χ^2 statistic. The magnitude of the statistic is always too high for an acceptable model even though the fits are qualitatively reasonable. We use this weighting-factor equation to provide a balanced contribution between constant and scaling uncertainties.

Unidimensional 95% confidence intervals for the gA parameters and coupling constants were obtained as single tails of the cumulative distribution function for the F statistic. Maple 9.5 was used to obtain the cutoff value of F (1.137) that would give $P < 0.05$ for 654 degrees of freedom (675 conductivity data points and 20 free parameters). Specifically, the upper and lower bounds for a parameter were taken as the value of that parameter that would produce a (reduced) χ^2 that was 1.137 times that of the optimal (reduced) χ^2. In calculating these uncertainties, the nonconductance data points were not considered.

Sensitivity analysis for the gA fit was performed by generating contour plots of the χ^2 surface with respect to rate-constant parameters. Two of the rate constants for one of the experimental paradigms, gA/K^+/DPhPC, were systematically varied while the remaining 12 parameters were held constant. χ^2 was calculated by comparing measured and predicted channel currents and does not include errors related to 3B2S predictions of the nonconductance measurements.

gM kinetic theory

The gM parameters, relative to the gA 3B2S parameters described above, were refined to simultaneously account for a broad set of published single-channel, Cs^+- and K^+-current data (5,18,25,29,46–49). The coupling constants for Cs^+ passage through gA were simultaneously calculated because most of the gM measurements were Cs^+ currents. The same Cs^+ coupling constants were applied to both gA and gM data. Again, χ^2 error minimization with uncertainty weights derived from the standard-deviation equation given as Eq. 1 was used to compute the gM parameters. Of particular interest here were the gA → gM coupling constants. Included in this ''gM fit'' were current-concentration data for gA/gM heterodimer channels. There were no gM nonconductance measurements available from the literature to serve as constraints in the fit, and the constraint that the second association rate constant equal the first was lifted with minor effects.

The gM coupling constants thus derived were used to calculate the differences in the free-energy profiles of gA and gM. The difference between

ΔG_{gA} and ΔG_{gM}, the free-energy barriers related to each of the rate constants ($X = A, B, K, D$, or E), was given as:

$$\Delta\Delta G_X = \Delta G^X_{gA} - \Delta G^X_{gM} = -RT\ \ln(X_{gA}/J) + RT\ \ln(X_{gM}/J) = RT\ \ln(CC^X_{gM}), \quad (2)$$

where J is the rate-theory prefactor. Because we use a perturbation methodology, it is irrelevant whether an Eyring, Kramers, or other prefactor is used, because the above relation does not depend on the prefactor J. The differences between the gA and gM free-energy profiles at each barrier and well were calculated from the gM coupling constants.

Combination rules relating heterodimer kinetics to homodimer kinetics; gM fitting weights

Heterodimers were assumed to have the same entry- and exit-rate constants as homodimers because the Trp side chains from the far side of the channel should have little energetic effect at the near ion-binding site (49). The heterodimer translocation rate constant was assumed to be related to the homodimer translocation rate constant in a way that can be derived from rate theory, based initially on the supposition that the energy at the center of the channel would contain the Trp profile from the gA side alone plus the height of the gM translocation energy barrier.

To determine the energy profile of the heterodimer channel, an apparent energy barrier (ΔG_i) was first calculated for each zero-voltage rate constant using a prefactor, J_i, for both gA and gM. These apparent energy barriers were then used to compile homodimer (symmetrical) free-energy profiles for each peptide variant. To obtain the free-energy profile of a heterodimer channel, the free-energy profiles for entry and exit in each constituent were combined into one composite profile. The heights of the translocation barriers of the two constituent homodimer free-energy profiles were averaged to produce the height of the heterodimer translocation barrier. This composite free-energy profile was then converted back into rate constants via Eyring rate theory using the same J_i as above, thus making the actual value of this prefactor unimportant in the calculation.

Ultimately, improved fits to the data were obtained by slight adjustments to the height and position of the heterodimer translocation barrier. These are parameterized as ω, which, if positive, shifts the location of the central barrier toward the gA side of the heterodimer, and λ, which weights the central barrier height. When $\lambda = 0$ or $\lambda = 1$, the central barrier for the heterodimer profile is equal to the height of the gA or gM central barrier, respectively, whereas $\lambda = 0.5$ represents a simple average, as one would expect if the four Trp residues from each side of the channel contribute equally to the ion free energy at the peak of the translocation barrier.

Because the heterodimer data serves as a unique test of any gM coupling-constant parameter set, it was given more weight than the other data during the process of fitting. Specifically, the new gM homodimer data was given a weight five times greater than any other data set (i.e., the contribution to χ^2 was increased fivefold), and the new gAgM/DPhPC and gMgA/DPhPC data were weighted by a factor of 10. Because the current-voltage relation superlinearity also depends on the height of the central barrier, it was also expected to constrain the rate of translocation. For this reason, superlinear gM/Cs^+ channel-current measurements from Heitz et al. (25) were given twice the weight of most other data sets in this fit to ensure that the 3B2S parameter set accurately predicted this distinctive superlinear relation. In contrast, two Heitz paradigms (25,48) showed strange secondary-rise behavior at very low voltages that could not be predicted with the 3B2S method. Because measurements made at low voltages may be less reliable, these data were given half the normal weight.

Unidimensional 95% confidence intervals for the gM parameters and coupling constants were obtained with the F-test method used for gA. The upper and lower bounds for a parameter were taken as the value of that parameter that would produce a (reduced) χ^2 that was 1.223 times that of the optimal (reduced) χ^2, which, with 285 conductivity data points and 15 free parameters (269 degrees of freedom), would occur with $P < 0.05$. Maple 9.5 was used to obtain the cutoff value of F for this large number of degrees of freedom.

Sensitivity analysis for gM and gM/gA fits were calculated using the same approach as was used for gA, described above. The weights for different data sets were equalized to eliminate any bias introduced by the weighting procedure.

RESULTS

Single gA homodimer channel currents: model parameterization

Table 1 shows the newly derived set of 3B2S rate constants and voltage-dependency parameters for gA based on a fit of all available published conductance data for Na^+ and K^+ in GMO/hexadecane and DPhPC/decane bilayers (3,5,8, 19–20,23,28–29,38,46–47,38,50–51). The results, although obtained independently of previous fits, are similar in many ways to published kinetic models, though we believe our current fit is more accurate because of the large number of data points considered. Second-ion exit is faster than first-ion exit by an order of magnitude, making first-ion exit rate-limiting at low ion concentrations (<0.1 M). Translocation becomes rate-limiting at high ion concentrations (>1.0 M) in DPhPC bilayers, but not in GMO bilayers, where translocation is nearly an order of magnitude faster. The fact that translocation in GMO is significantly faster than in DPhPC is expected because the height of the interfacial dipole potential barrier is ~1.5 kcal/mol greater in DPhPC than in GMO (see discussions in Cole et al. (8) and Duffin et al. (30)). The first voltage-dependent parameter, α_1, is close to zero, suggesting that the rate of entry is not very voltage-dependent in gA. Rather than an energy barrier, the entry step in the current model is envisioned to represent diffusion through the

TABLE 1 Gramicidin A 3B2S parameters

Rate constants	A (M^{-1} s^{-1})	B (s^{-1})	K (s^{-1})	D (M^{-1} s^{-1})	E (s^{-1})
DPhPC, K^+, gA	1.7 (1.2–2.1) × 10^8	2.3 (−0.4–4.4) × 10^6	1.7 (1.4–2.1) × 10^7	1.7 (1.5–1.7) × 10^8	3.9 (3.6–4.4) × 10^7
Coupling constants	A	B	K	D	E
DPhPC → GMO	0.89 (0.56–1.3)	0.45 (−0.17–0.90)	9.2 (6.4–15.0)	0.89 (0.77–0.94)	0.77 (0.67–0.88)
$K^+ \rightarrow Na^+$	0.46 (0.27–0.77)	0.70 (−0.36–1.48)	0.53 (0.42–0.78)	0.46 (0.37–0.49)	0.54 (0.46–0.63)
Voltage-dependency parameters			$\alpha 1$		$\alpha 2$
DPhPC			0.021 (0.007–0.033)		0.101 (0.083–0.119)
GMO			0.030 (0.015–0.043)		0.231 (0.195–0.270)

Values in parentheses are 95% confidence intervals.

hemispherical access resistance. The second voltage-dependent parameter, α_2, which specifies the location of the binding sites, is consistent with the position of ion binding from NMR (35–36) and x-ray diffraction (37) studies. The 3B2S-predicted binding affinities (A/B) reported here for the two ions in question vary qualitatively according to their dehydration energies and, together with the second ion affinities, are similar to those measured with NMR techniques (44,52).

Unidimensional 95% confidence intervals based on the F-test were obtained from the conductivity data alone, with the assumption that all reported measurements were independent samples, even though a few represent identical conditions derived from different labs. The confidence intervals do not reflect correlation between parameters, and in this sense are a crude estimate of the uncertainty in any given parameter, but at least illustrate the relative importance of the different parameters to the fit. The exit-rate constants from kinetic modeling are known to be weakly constrained by conductivity data (47), so we have further constrained them with binding affinity and other nonconductance data. The previously published and fitted values obtained for some of these additional nonconductance constraints are shown in Table 2. The net uncertainties in the exit-rate constants are dramatically reduced by this procedure, probably to below the levels of the uncertainty in the measured tight and weak binding constants (average fitting error of 1.7% for the second-ion binding constant and 12.2% for the first-ion binding constant (44)), because the association rate constants are quite well established, both statistically from the fit and with high-voltage maximum conductance results (5).

Fig. 1 compares measured gA currents from various labs to those currents predicted by the 3B2S model, separated according to lipid and ion species. The 3B2S parameter set not only predicts measured channel currents but also the nonconductance measurements listed in Table 2. Error bars for the data are omitted because they are generally smaller than the size of the symbols. Careful inspection of the data points, which are color-coded according to concentration and symbol-coded according to lab, shows the good agreement between labs for different concentrations. Conductances are generally lower in DPhPC bilayers than in GMO bilayers by a factor of ~2. Although difficult to visualize, the fits are reasonable throughout. Some systematic weaknesses in the current-voltage shape can be seen, for instance, in the predicted superlinearity for 2 M KCl in DPhPC bilayers (Fig. 1 *a*). These were partly induced by the application of the nonconductance data constraints.

Fig. 2 shows contour plots of the χ^2 surface with respect to rate-constant parameters for sensitivity analysis. χ^2 was calculated by comparing measured and predicted channel currents and does not include errors related to 3B2S predictions of the nonconductance measurements listed in Table 2. The symbol, ×, which marks the values of the current parameter set, always lies at or near the minimum of the χ^2 surface, indicating that the nonconductance measurements were reasonably compatible with the conductivity measurements. These plots indicate that K, the rate of translocation, is well constrained relative to A (Fig. 2 *a*) and B (Fig. 2 *b*), that D is constrained relative to A (Fig. 2 *c*), and that E is highly constrained relative to B (Fig. 2 *d*). Although the fact that the measured maximal voltage conductance at low ion concentration yields an A similar to the well-constrained D dictated that A and D be constrained to be equal to reduce freedom in the fitting procedure, Fig. 2 *c* indicates that the conductivity data themselves do not require that equality. A can be increased slightly without increasing χ^2 much, as long as D is decreased to compensate.

Single heterodimer channel current measurements

Single-channel currents had two principle conductance levels (Fig. 3 *a*) when gA was added to the *cis* chamber (held electrically negative relative to the *trans* chamber) after DPhPC bilayer formation between two chambers containing gM. The lowest conductance corresponded exactly to gM homodimer channels measured in the absence of gA and was therefore assigned to be the gM homodimer peak. The next higher conductance dominated early in the experiment after adding gA to the *cis* chamber for a membrane preloaded symmetrically with gM, and was therefore interpreted to be composed of a gA molecule in the *cis* (exit) leaflet and a gM molecule in the *trans* (entrance) leaflet, i.e., gMgA heterodimers. By the time of this sample (~10 min of data collection), a few of the second type of heterodimers had begun to appear, presumably because some gA monomers had transferred to the *trans* leaflet and were forming heterodimers with gM molecules in the *cis* leaflet. These were therefore taken to be gAgM heterodimers.

TABLE 2 Gramicidin A: 3B2S predictions of experimental observables

	GMO			DPhPC		
	Na^+	K^+	Cs^+	Na^+	K^+	Cs^+
$A \times 10^{-8}$ M^{-1} s^{-1}	0.67 (1.0)	1.5 (1.9)	(2.1)	0.76 (1.1)	1.7 (1.7)	(1.6)
$K_1 = A/B$ M^{-1}	92 (46)	146 (73)	(95)	46.1 (46)	70.8 (73)	(95)
$K_2 = D/E$ M^{-1}	5.3 (4.8)	4.0 (3.6)	(4.8)	3.6 (4.8)	4.2 (3.6)	(4.8)

Values in parentheses are targets from the literature (39,44) used as constraints. Flux ratio exponents (45), ion binding positions (37), and lipid coupling constants (30) were also constrained. The experimental Cs+ parameters are included for comparison, although they were only used indirectly, i.e. for gramicidin M fits (see Table 3).

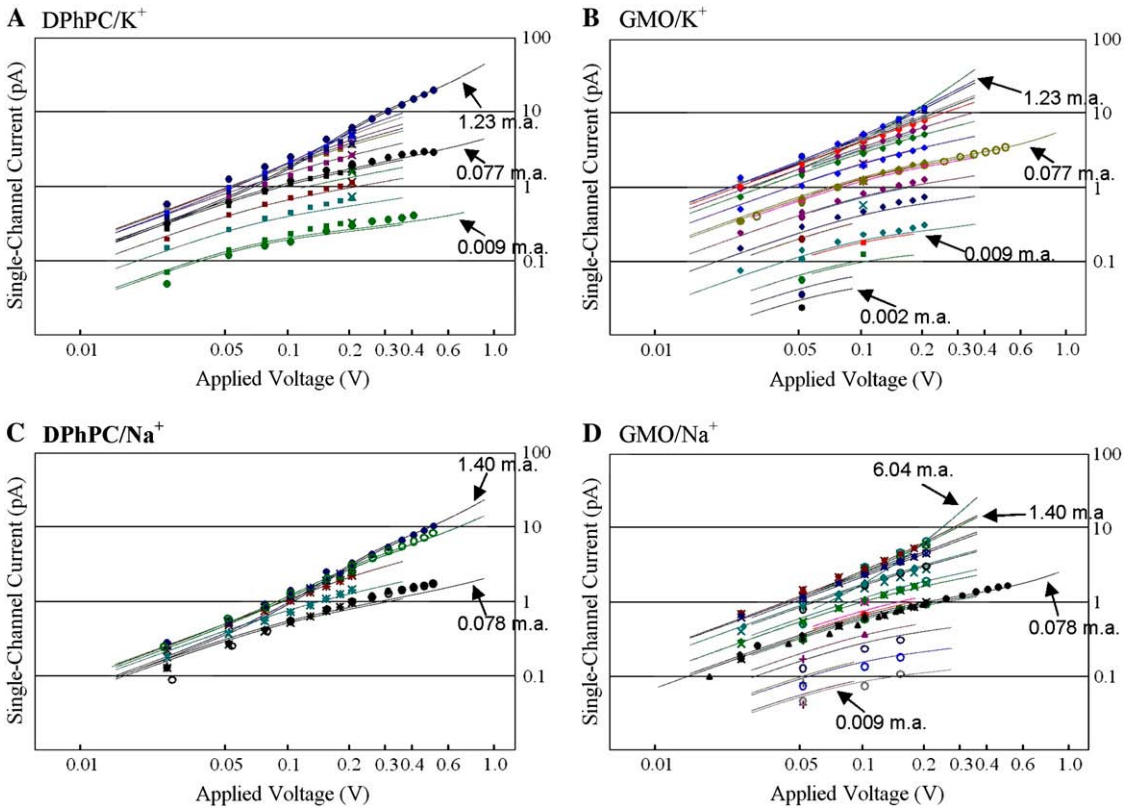

FIGURE 1 Single-channel current-voltage relations (*points*) and model predictions (*solid curves*) for previously published experiments with gramicidin A at different molal activities (*m.a.*). Despite the many constraints placed on the parameter set (including the requirement that the set accurately predict binding constants, flux ratio exponents, and channel-current measurements under various conditions), the model is successful in predicting channel current. Error bars are omitted because the errors are generally smaller than the size of the symbols. Data points are color-coded by concentration using the same color scale as the theoretical curves. Current-voltage data is given for measurements reported in the references as follows: (*a*) DPhPC/K^+, ● (5,38,39); ■ (8); × (29); (*b*) GMO/K^+, ● (46); ■ (47); × (51), + (29); ○ (5); ▲ (50); ♦ (8); (*c*) DPhPC/Na^+, ● (5); ■ (19); × (20); + (23); ○ (28); (*d*) GMO/Na^+, ● (5); ■ (50); × (20); + (46), ○ (47); ▲ (51); ♦ (23).

Fig. 3 *b* shows a histogram from an experiment where both peptides were applied to both chambers. Two additional peaks appear in this case. One has the same conductance as the gMgA peak found in an experiment in GMO (and otherwise similar to that shown in Fig. 3 *a* above). The other has the conductance measured in GMO bilayer experiments using only gA, and was therefore taken to be a gA homodimer peak. Experiments similar to that shown in Fig. 3 *b* were conducted at various KCl concentrations; composite histograms were created, and peaks were assigned in the same sequence for each concentration.

gM kinetic theory

The 3B2S gM coupling constants that correspond to the best fit of the data are presented in Table 3. Here, in addition to gM homodimer and gM/gA heterodimer conductance data, coupling constants for Cs^+ were determined that simultaneously predicted the gA homodimer Cs^+ conductance and binding-affinity data. We found that in the context of the gA homodimer data alone, the Cs^+ parameters were poorly constrained, but that the added constraint of having to fit the gM-related data allowed good definition of the Cs^+ coupling constants, as is evidenced by the 95% confidence intervals in Table 3. For this gM fit, the assumption of equality between *A* and *D* was relaxed to improve the fits with only minor consequences to the parameters. The principle and most certain difference between the gA and gM rate constants (as measured by the unidimensional 95% confidence interval) is an ~100-fold decrease in translocation passage rate, *K*, in gM. There are also small decreases in both first- and second-ion entry, rates *A* and *D*, and large increases in first- and second-ion exit, rates *B* and *E*, in gM. The confidence intervals indicate, however, that although CC^{B}_{gM} and CC^{E}_{gM} are generally large, they are not as well constrained by the gM data as are the gA lipid and ion coupling constants. CC^{B}_{gM} and CC^{E}_{gM} are probably only weakly constrained because the first and second rates of exit in gM are very fast compared to gA (as evidenced by large values of CC^{B}_{gM} and CC^{E}_{gM}) and so are never rate-limiting. Because predicted current is most dependent on the rate-limiting step, it is far more difficult to obtain exact values for the faster rate constants.

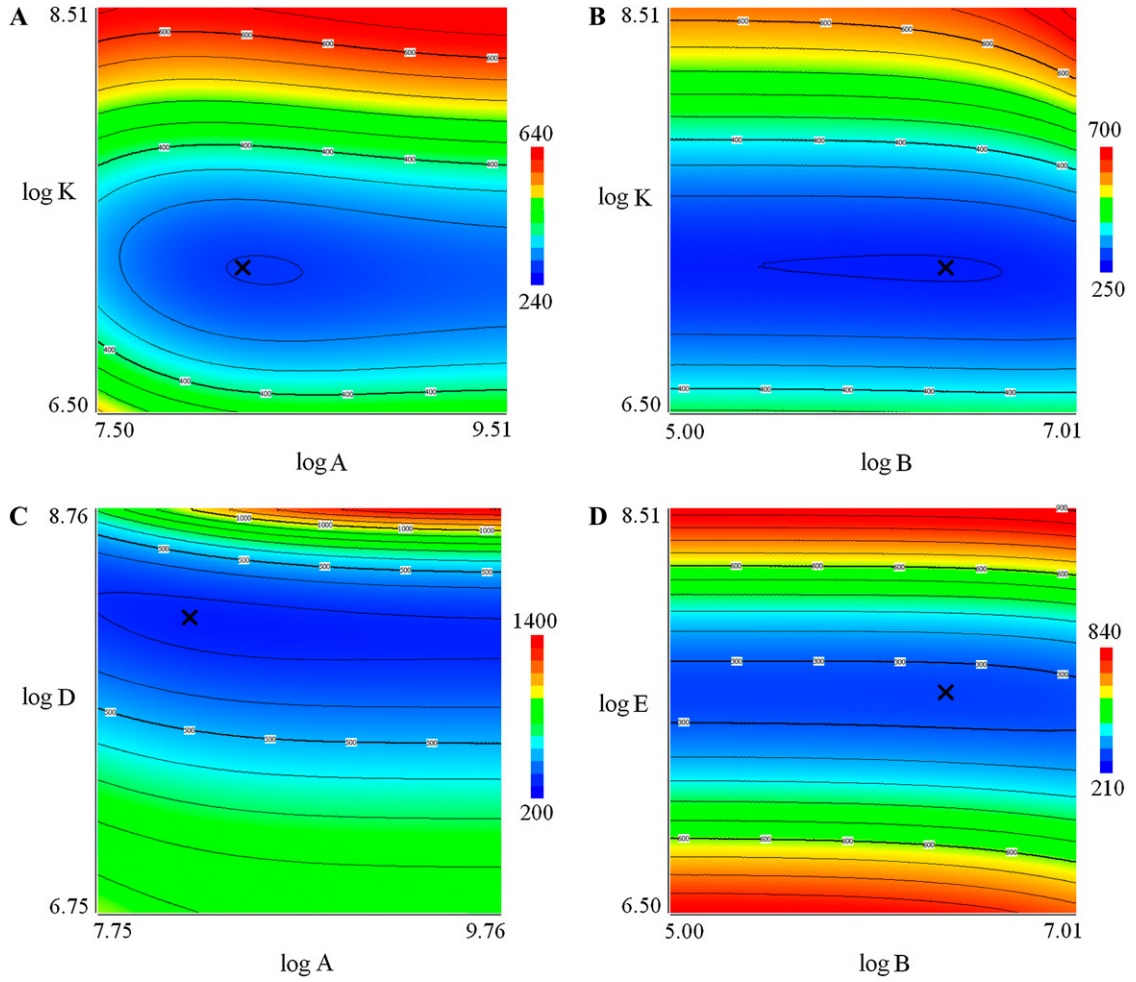

FIGURE 2 Contour plots of the χ^2 surface with respect to rate-constant parameters provide an estimate of their uncertainty. Here, the rate constants from the basis set (gA/K^+/DPhPC) were varied systematically around the values of the current parameter set. Colors represent the χ^2 goodness-of-fit statistic. Although the magnitude of this statistic is not directly meaningful because of its dependence on our assumption of very high precision and reproducibility between labs as well as on the arbitrary weights assigned to the nonconductance data, it provides an indication of the relative dependence of the quality of the fits on the different parameters. Aside from the pair of parameters varied in each plot, all other parameters were held constant. Notice that the ×, which marks the values of the current parameter set, always lies at or near the minimum of the χ^2 surface. (*a*) Plot of the χ^2 surface as first-ion rate of entry and rate of translocation are varied about the values of the current parameter set. (*b*) Plot of the χ^2 surface as first-ion rate of exit and rate of translocation are varied about the values of the current parameter set. (*c*) Plot of the χ^2 surface as first- and second-ion rate of entry are varied about the values of the current parameter set. (*d*) Plot of the χ^2 surface as first- and second-ion rate of exit are varied about the values of the current parameter set.

Fig. 4 compares measured gM/Cs^+ and gA/Cs^+ currents to those currents predicted by the 3B2S model. Fig. 4, *a* and *g*, shows gM homodimer data, Fig. 4, *b–f*, shows gA homodimer Cs^+-current data, and Fig. 4, *h–i*, shows plots of our previously published and new gM-gA heterodimer data. In these two plots, the gA homodimer results taken from the same experiments are not shown, as they were included in Fig. 1. gM homodimer results are included for comparison to the other gM homodimer results in Fig. 4, *a* and *g*. The strong superlinearity in the current-voltage relations (Fig. 4 *g*), as well as the self-block at low voltage (Fig. 4 *a*), for the gM homodimers is well predicted by the 3B2S model. Although some systematic variations in curve shape are seen in these fits, as well as in the new gM homodimer data in Fig. 4, *h* and *i*, they are similar in level of discrepancy to gA homodimer fits and so were considered to be tolerable deviations. The constrained combination of gA and gM parameters provide an acceptable fit of the heterodimer data in Fig. 4, *h* and *i*.

The very small coupling constant for the translocation step in gM channels was critical for this success. The 3B2S model predictions of the degree of ''heterodimer peak splitting'', i.e., the difference in the conductance of the two heterodimer orientations, was strongly dependent upon the rate-limiting step. If the rate-limiting step is near the center of the channel, where the two orientations would differ the least, the splitting is small, whereas if it is at the entry or exit, the splitting is very large (data not shown). In the data presented in Fig. 4, *h* and *i*, the splitting is relatively small, so we conclude that translocation is the dominant rate-limiting step from that qualitative observation alone.

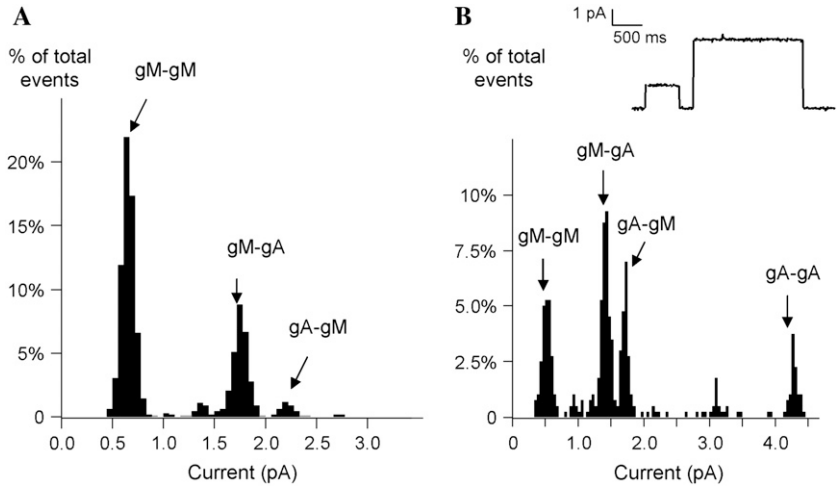

FIGURE 3 (*a*) Single-channel current histogram with gM added to both sides of the DPhPC membrane and gA added to only one side (*cis*), forming gM-gA channels. Some gA peptides do cross the bilayer, producing a few gA-gM channels. The highest peak represents gM homodimer channels. The orientation of the heterodimer channel is assigned based on the known low gA transfer rate across the membrane. 1.0 KCl, DPhPC. (*b*) Histogram and single-channel current trace in GMO. 1.0 M KCl, gM and gA on both sides of the membrane at 100 mV. Peaks are labeled according to an experiment like that shown in *a*, but with GMO bilayers. Reprinted with permission from Caywood and Busath (29).

Fig. 5 shows contour plots of the χ^2 surface with respect to coupling-constant parameters, which provide an estimate of the uncertainty in those parameters. Notice that the $\times$ in each plot, which marks the values of the current parameter set, always lies at or near the minimum of the χ^2 surface. In calculating this χ^2 surface, each data point was weighted equally. These plots indicate that the gM coupling constant for the rate of translocation, CC^{K}_{gM}, must be small (Fig. 5 *b*), and that the coupling constant for the first-ion rate of entry, CC^{A}_{gM}, is not well constrained by CC^{K}_{gM} (Fig. 5 *a*). Likewise, the coupling constant for the first-ion rate of exit, CC^{B}_{gM}, is not well constrained with respect to CC^{K}_{gM} (Fig. 5 *b*). This apparent lack of constraints on CC^{A}_{gM} and CC^{B}_{gM} is resolved, however, in Fig. 5 *c*, which shows that CC^{A}_{gM} is well constrained by the coupling constant for the second-ion rate of entry, CC^{D}_{gM}, and Fig. 5 *d*, which shows that CC^{B}_{gM} is constrained by the coupling constant for the second-ion rate of exit, CC^{E}_{gM}. Furthermore, Fig. 5, *c* and *d*, also indicates that CC^{D}_{gM} and CC^{E}_{gM} are well constrained. Although the χ^2 plots corresponding to only four out of 120 possible parameter pairs are shown here, these four alone show that all gM coupling constants are reasonably well constrained.

Fig. 6 compares the free energy of the first-ion gA-gM difference (found by converting the gM coupling constants to energy differences via Eyring rate theory) to the dynamic average axial Trp potential using the Charmm22/27 force field (transcribed from Woolf and Roux (53)). We found that only a bowl-shaped Trp energy profile would produce the gM coupling constants required to fit both heterodimer and superlinear current-voltage data because it alone allows the rate of passage through the channel to be increased in gA over gM, yielding predicted gA currents that are higher than gM currents, as observed experimentally. The bowl-shaped profile is also consistent with previous fits of current-voltage relations (24) and of responsiveness to interfacial agents (30). Note that although Woolf and Roux did not calculate the Trp potential near the channel center, the portion of the profile they did calculate is sufficient to demonstrate a double-nadir shape.

DISCUSSION

As mentioned previously, gM is an analog of gA in which the four gA-Trp residues are replaced with Phe. Replacement of Trp side chains with nonpolar residues like Phe inhibits alkali cation current flow through gramicidin channels (18,24–30). The shapes of current-voltage relations (24) and responsiveness to interfacial agents (30) suggest that the addition of the Trp profile to the underlying free-energy profile for ion passage through gM might enhance current in

TABLE 3 3B2S parameters from gramicidin M and heterodimer fits

Coupling constants	*A*	*B*	*K*	*D*	*E*
$K^+ \rightarrow Cs^+$	0.62 (0.30–1.01)	0.46 (0.14–3.11)	1.01 (0.79–1.17)	1.30 (1.03–1.57)	3.1 (2.1–4.3)
gA $\rightarrow$ gM	0.84 (0.32–1.29)	23.5 (12.8–97.6)	0.010 (0.008–0.012)	0.68 (0.24–1.04)	10.2 (4.9–38.4)
gM voltage-dependency parameters			$\alpha 1$		$\alpha 2$
DPhPC			0.000 (−0.151–0.119)		0.145 (0.062–0.213)
GMO			0.017 (−0.026–0.070)		0.168 (0.139–0.207)
Heterodimer parameters					
λ					0.48 (0.42–0.57)
ω					0.13 (0.04–0.20)

Values in parentheses are 95% confidence intervals.

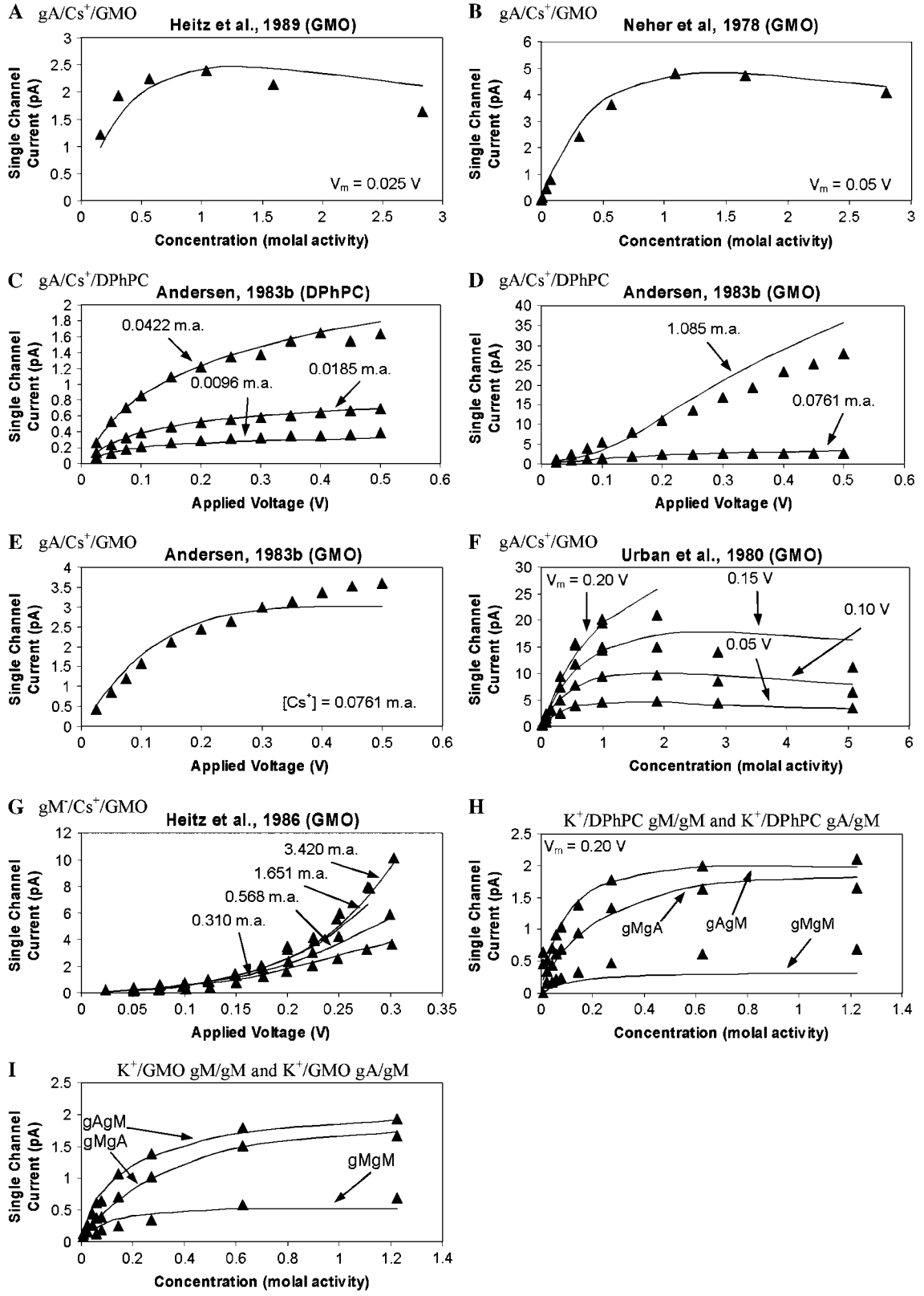

FIGURE 4 Measured and predicted current-voltage-concentration relations for gM. Despite the many constraints placed on the parameter set (particularly the requirement that the prediction be accurate both for the heterodimer channel currents and superlinear current-voltage measurements), the model is generally successful in predicting channel current. Error bars are omitted, because the errors used, given by the Thompson standard-deviation equation, $W(pA) = 0.0143\bar{i}(pA) + 0.0026pA$, are smaller than the size of the symbols. The concentrations are here reported in molal activity (*m.a.*), which is the concentration

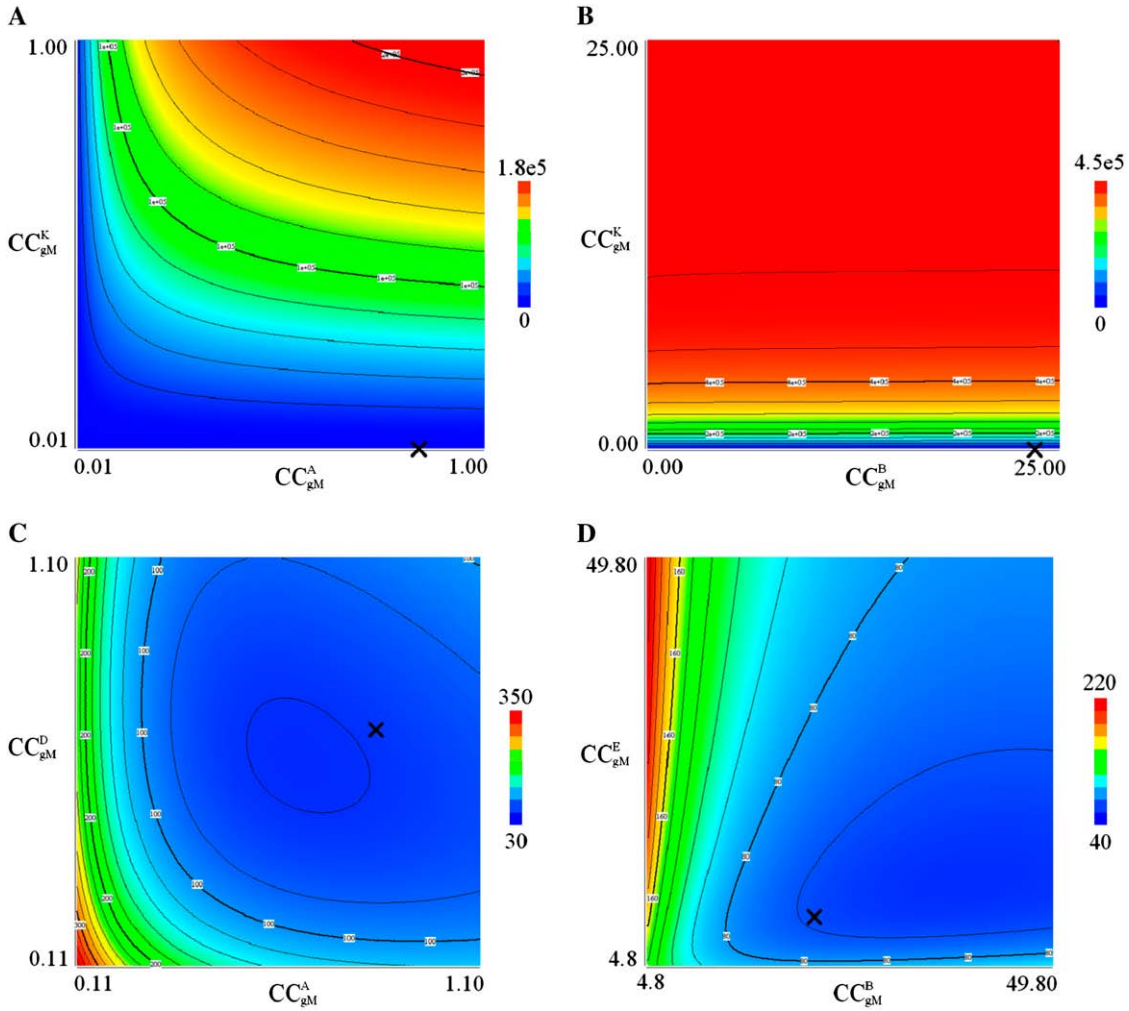

FIGURE 5 Contour plots of the χ^2 surface with respect to coupling-constant parameters provide an estimate of their uncertainty. Here, the gM rate constants were varied systematically around the values of the current parameter set. Colors represent the χ^2 goodness-of-fit (assuming 14 free parameters), an indication of how well our model predicts observed gramicidin conductance. Aside from the pair of parameters varied, all other parameters were held constant. Notice that the $\times$, which marks the values of the current parameter set, always lies at or near the minimum of the χ^2 surface. (*a*) Plot of the χ^2 surface as the coupling constants on the first-ion rate of entry, *A*, and rate of translocation, *K*, are varied about the values of the current parameter set. (*b*) Plot of the χ^2 surface as the coupling constants on first-ion rate of exit, *B*, and rate of translocation, *K*, are varied about the values of the current parameter set. (*c*) Plot of the χ^2 surface as the coupling constants on first- and second-ion rate of entry, *A* and *D*, are varied about the values of the current parameter set. (*d*) Plot of the χ^2 surface as the coupling constants on first- and second-ion rate of exit, *B* and *E*, are varied about the values of the current parameter set.

gA by increasing the rate of passage through the channel in a translocation-limited situation.

We found that only a bowl-shaped Trp energy profile would produce the gM coupling constants required to fit both heterodimer and superlinear current-voltage data. This shape contrasts with the double-nadir molecular-dynamics-derived Trp electrostatic potential from Woolf and Roux (53), calculated using the Charmm22/27 force field. Although it is possible that differences in gM channel structure, dynamics, or electrostatics of the Phe side chain could be responsible

FIGURE 4 (Continued).
in molal multiplied by the corresponding activity coefficient. The model adequately predicted four channel current measurements from Fonseca et al. (18), not shown here. Two Heitz paradigms (25,48) showed strange secondary-rise behavior at very low voltages that was difficult to predict with the 3B2S method. Because measurements made at low voltages may be less reliable, these two data sets were given a weight that was half that of most other data sets included in this fit and are not shown here. (*a*) gA/Cs^+/GMO measurements from Heitz et al. (48). (*b*) gA/Cs^+/GMO measurements from Neher et al. (46). (*c*) gA/Cs^+/DPhPC measurements from Andersen (38). (*d*) gA/Cs^+/DPhPC measurements from Andersen (38). (*e*) gA/Cs^+/GMO measurements from Andersen (38). (*f*) gA/Cs^+/GMO measurements from Urban et al. (47). Note that some points, omitted from this graph, were included in the fit. (*g*) gM^-/Cs^+/GMO measurements from Heitz et al. (25). (*h*) K^+/DPhPC gM homodimer and K^+/DPhPC gA/gM heterodimer measurements from Caywood and Busath (29). (*i*) K^+/GMO gM homodimer and K^+/GMO gA/gM heterodimer measurements from Caywood and Busath (29).

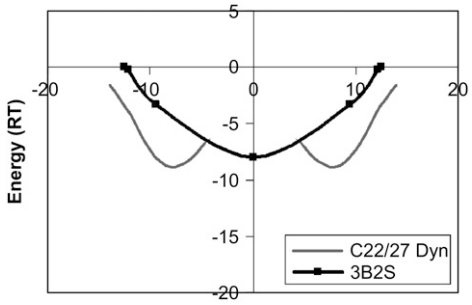

FIGURE 6 Comparison of the free energy of the first-ion gA-gM difference (*blue*) and the dynamic average axial Trp potential using the Charmm22/27 force field (*gray*, transcribed from Woolf and Roux (53)). We found that only a bowl-shaped Trp energy profile would produce the gM coupling constants required to fit both heterodimer and superlinear current-voltage data because it alone allows the rate of passage through the channel to be increased in gA over gM, yielding predicted gA currents that are higher than gM currents, as observed experimentally. The bowl-shaped profile is also consistent with previous fits of current-voltage relations (24) and of responsiveness to interfacial agents (30). Note that although Woolf and Roux did not calculate the Trp potential near the channel center (53), the portion of the profile they did calculate is sufficient to demonstrate a double-nadir shape.

for this discrepancy, we assume for the purposes of this discussion that Trp electrostatics are the primary determinant of this energy profile. In this case, rate theory would predict that in the double-nadir profile case the gA ion exit rates, B and E, and the gA translocation rate, K, would be smaller than in gM. gM currents would consequently be higher than gA currents, contrary to observation. This problem may be partly alleviated if the Phe potential in gM channels is nonzero, but we have not explored this possibility here for lack of information about the Phe side-chain structures and dynamics in gM. We have carried out additional calculations for the Trp electrostatic potential of the static gramicidin structure (12) using partial charges from seven other nonpolarizable force fields, which produced both double-nadir and bowl-shaped Trp potentials (data not shown). Although these electrostatic results lack consideration of correlations between the ion position and the Trp side-chain configuration, as well as potential nonelectrostatic contributions of the Trp side chains to the axial free-energy profile, they do suggest that free energy perturbation or umbrella-sampling molecular-dynamics simulations may help distinguish force-field models for the Trp side chain in the future.

The bowl-shaped energy difference derived here from rate-theory analysis of experimental data, in which the rate of passage through the channel, K, is increased in gA over gM, results in gA currents being higher than gM currents. Such a bowl-shaped profile is also consistent with previous fits of current-voltage relations (24) and of responsiveness to interfacial agents (30).

To evaluate the statistical level of confidence in the 3B2S-derived gA-gM difference free-energy profile, it is helpful to consider Table 3. Assuming the true value of each gM coupling constant lies in the unidimensional 95% confidence interval defined in Table 3, we computed $\Delta\Delta G_X$ from CC^X_{gM} according to Eq. 2. Using this technique, we see that $-1.1\,RT \le \Delta\Delta G_A \le 0.3\,RT$, $2.5\,RT \le \Delta\Delta G_B \le 4.6\,RT$, $-4.9\,RT \le \Delta\Delta G_K \le -4.5\,RT$, $-1.4\,RT \le \Delta\Delta G_D \le 0.0\,RT$, and $-1.6\,RT \le \Delta\Delta G_E \le -3.6\,RT$. Clearly the gM coupling constant most accurately known is that associated with the rate of translocation, CC^K_{gM}, which is reduced ~100-fold in gM over gA.

CONCLUSION

In this article, we built upon our previous research into the transport kinetics of gA and gM by considering the difference between the 3B2S-predicted free-energy profiles of each. The 3B2S-predicted Trp profile is bowl-shaped, suggesting a manifold reduction in the rate of translocation in gM as compared with gA. Assuming the ratios of rate constants to be related to the free-energy difference between gA and gM, we construct an effective ion-Trp free-energy interaction profile that has a minimum at the channel center.

REFERENCES

1. Hladky, S. B., and D. A. Haydon. 1972. Ion transfer across lipid membranes in the presence of gramicidin A. Studies of the unit conductance channel. *Biochim. Biophys. Acta*. 274:294–312.
2. Bamberg, E., and P. Lauger. 1973. Channel formation kinetics of gramicidin A in lipid bilayer membranes. *J. Membr. Biol.* 11:177–194.
3. Neher, E. 1975. Ionic specificity of the gramicidin channel and the thallous ion. *Biochim. Biophys. Acta*. 401:540–544.
4. Sandblom, J., G. Eisenman, and E. Neher. 1977. Ionic selectivity, saturation and block in gramicidin A channels. I. Theory for the electrical properties of ion selective channels having two pairs of binding sites and multiple conductance states. *J. Membr. Biol*. 31: 383–417.
5. Andersen, O. S. 1983a. Ion movement through gramicidin A channels. Single channel measurements at very high potentials. *Biophys. J*. 41: 119–133.
6. Busath, D., and G. Szabo. 1981. Gramicidin forms multi-state rectifying channels. *Nature*. 294:371–373.
7. Cukierman, S., E. P. Quigley, and D. S. Crumrine. 1997. Proton conduction in gramicidin A and in its dioxolane-linked dimer in different lipid bilayers. *Biophys. J*. 73:2489–2502.
8. Cole, C. D., A. S. Frost, N. Thompson, M. Cotten, T. A. Cross, and D. D. Busath. October. 2002. Noncontact dipole effects on channel permeation. VI. 5F and 6F Trp gramicidin channel currents. *Biophys. J*. 83:1974–1986.
9. Shirts, M. R., J. W. Pitera, W. C. Swope, and V. S. Pande. 2003. Extremely precise free energy calculations of amino acid side chain analogs: comparison of common molecular mechanics force fields for proteins. *J. Chem. Phys.* 119:5740–5761.
10. Urry, D. W., J. D. Glickson, D. F. Mayers, and J. Haider. 1972. Spectroscopic studies on the conformation of gramicidin A′. Evidence for a new helical conformation. *Biochemistry*. 11:487–493.
11. Arseniev, A. S., A. L. Lomize, I. L. Barsukov, and V. F. Bystrov. 1985. 1H-NMR study of gramicidin A transmembrane ion channel. Head-to-head right-handed, single-stranded helices. *FEBS Lett*. 186:168–174.
12. Ketchem, R. R., B. Roux, and T. A. Cross. 1997. High-resolution polypeptide structure in a lamellar phase lipid environment from solid state NMR derived orientational constraints. *Structure*. 5:1655–1669.
13. Townsley, L. E., W. A. Tucker, S. Sham, and J. F. Hinton. 2001. Structures of gramicidins A, B, and C incorporated into sodium dodecyl sulfate micelles. *Biochemistry*. 40:11676–11686.

14. Myers, V. B., and D. A. Haydon. 1972. Ion transfer across lipid membranes in the presence of gramicidin A. II. The ion selectivity. *Biochim. Biophys. Acta.* 274:313–322.

15. Durkin, J. T., R. E. Koeppe II, and O. S. Andersen. 1990. Energetics of gramicidin hybrid channel formation as a test for structural equivalence. Side-chain substitutions in the native sequence. *J. Mol. Biol.* 211:221–234.

16. O'Connell, A. M., R. E. Koeppe II, and O. S. Andersen. 1990. Kinetics of gramicidin channel formation in lipid bilayers: transmembrane monomer association. *Science.* 250:1256–1259.

17. Heitz, F., P. Daumas, N. Van Mau, R. Lazaro, Y. Trudelle, C. Etchebest, and A. Pullman. 1988. Linear gramicidins: influence of the nature of the aromatic side chains on the channel conductance. *In* Transport Through Membranes: Carriers, Channels, and Pumps. A. Pullman, J. Jortner, and B. Pullman, editors. Kluwer Academic Publishers, Dordrecht, The Netherlands. 147–165.

18. Fonseca, V., P. Daumas, L. Ranjalahy Rasoloarijjao, F. Heitz, R. Lazaro, Y. Trudelle, and O. S. Andersen. 1992. Gramicidin channels that have no tryptophan residues. *Biochemistry.* 31:5340–5350.

19. Becker, M. D., D. V. Greathouse, R. E. Koeppe II, and O. S. Andersen. 1991. Amino acid sequence modulation of gramicidin channel function: effects of tryptophan to phenylalanine substitutions on the single channel conductance and duration. *Biochemistry.* 71:83–88.

20. Busath, D. D., C. D. Thulin, R. W. Hendershot, L. R. Phillips, P. Maughn, C. D. Cole, N. C. Bingham, S. Morrison, L. C. Baird, R. J. Hendershot, M. Cotten, and T. A. Cross. 1998. Noncontact dipole effects on channel permeations. I. Experiments with (5F indole)Trp 13 gramicidin A channels. *Biophys. J.* 75:2830–2844.

21. Dorigo, A. E., D. G. Anderson, and D. D. Busath. 1999. Noncontact dipole effects on channel permeation. II. Trp conformations and dipole potentials in gramicidin A. *Biophys. J.* 76:1897–1908.

22. Phillips, L. R., C. D. Cole, R. J. Hendershot, M. Cotton, T. A. Cross, and D. D. Busath. 1999. Noncontact dipole effects on channel permeation. III. Anomalous proton conductance effects in gramicidin. *Biophys. J.* 77:2492–2501.

23. Thompson, N., G. Thompson, C. D. Cole, M. Cotten, T. A. Cross, and D. D. Busath. 2001. Noncontact dipole effects on channel permeation. IV. Kinetic model of 5F-Trp13 gramicidin A currents. *Biophys. J.* 81: 1245–1254.

24. Heitz, F., C. Gavach, and Y. Trudelle. 1984. Single channels of various gramicidins. Voltage effects. *Biophys. J.* 45:97–99.

25. Heitz, F., C. Gavach, G. Spach, and Y. Trudelle. 1986. Analysis of the ion transfer through the channel of 9,11,13,15-phenylalanylgramicidin A. *Biophys. Chem.* 24:143–148.

26. Durkin, J. T., O. S. Andersen, E. R. Blout, F. Heitz, R. E. Koeppe II, and Y. Trudelle. 1986. Structural information from functional measurements. Single channel studies of gramicidin analogs. *Biophys. J.* 49: 118–121.

27. Daumas, P., D. Benamar, F. Heitz, L. Ranjalahy-Rasoloarijao, R. Mouden, R. Lazaro, and A. Pullman. 1991. How can the aromatic sidechains modulate the conductance of the gramicidin channel? A new approach using non-coded amino acids. *Int. J. Pept. Protein Res.* 38:218–228.

28. Becker, M. D., R. E. Koeppe II, and O. S. Andersen. 1992. Amino acid substitutions and ion channel function. *Biophys. J.* 62:25–27.

29. Caywood, D., and D. D. Busath. 2002. Oriented gramicidin M gramicidin A heterodimers: rectification decreases with increased ion concentration. *In*: Membrane Interacting Peptides and Proteins. F. Heitz, editor. Research Signpost, Kerala, India. 147–153.

30. Duffin, R. L., M. P. Garrett, K. B. Flake, J. D. Durrant, and D. D. Busath. 2003. Modulation of lipid bilayer interfacial dipole potential by phloretin, RH421, and 6-ketocholestanol as probed by gramicidin channel conductance. *Langmuir.* 19:1439–1442.

31. Roux, B., and M. Karplus. 1993. Ion transport in the gramicidin channel: free energy of the solvated right-handed dimer in a model membrane. *J. Am. Chem. Soc.* 115:3250–3262.

32. Aqvist, J., and A. Warshel. 1989. Energetics of ion permeation through membrane channels. Solvation of Na+ by gramicidin A. *Biophys. J.* 56:171–182.

33. Allen, T. W., O. S. Andersen, and B. Roux. 2004. Energetics of ion conduction through the gramicidin channel. *Proc. Natl. Acad. Sci. USA.* 101:117–122.

34. Hu, W., and T. A. Cross. 1995. Tryptophan hydrogen-bonding and electric-dipole moments. Functional roles in the gramicidin channel and implications for membrane-proteins. *Biochemistry.* 34:14147–14155.

35. Urry, D. W., K. U. Prasad, and T. L. Trapane. 1982. Location of monovalent cation binding sites in the gramicidin channel. *Proc. Natl. Acad. Sci. USA.* 79:390–394.

36. Tian, F., K. C. Lee, W. Hu, and T. A. Cross. 1996. Monovalent cation transport: lack of structural deformation upon cation binding. *Biochemistry.* 35:11959–11966.

37. Olah, G. A., H. W. Huang, W. Liu, and Y. Wu. 1991. Location of ion binding sites in the gramicidin channel by x-ray diffraction. *J. Mol. Biol.* 218:847–858.

38. Andersen, O. S. 1983b. Ion movement through gramicidin A channels. Interfacial polarization effects on single channel current measurements. *Biophys. J.* 41:135–146.

39. Andersen, O. S. 1983c. Ion movement through gramicidin A channels. Studies on the diffusion controlled association step. *Biophys. J.* 41: 147–165.

40. Levitt, D. G. 1982. Comparison of Nernst-Planck and reaction-rate models for multiply occupied channels. *Biophys. J.* 37:575–587.

41. Urban, B. W., S. B. Hladky, and D. A. Haydon. 1978. The kinetics of ion movements in the gramicidin channel. *Fed. Proc.* 37:2628–2632.

42. Urry, D. W., T. L. Trapane, C. M. Venkatachalam, and K. U. Prasad. 1986. Energy profiles for sodium ion passage though the single filing gramicidin transmembrane channel. *Int. J. Quant. Chem. Quant. Biol. Symp.* 12:1–13.

43. Busath, D., and G. Szabo. 1988. Permeation characteristics of gramicidin conformers. *Biophys. J.* 53:697–707.

44. Jing, N., K. U. Prasad, and D. W. Urry. 1995. The determination of binding constants of micellar-packaged gramicidin A by 13C-and 23Na-NMR. *Biochim. Biophys. Acta.* 1238:1–11.

45. Procopio, J., and O. S. Andersen. 1979. Ion tracer fluxes through gramicidin A in modified lipid bilayers. *Biophys. J.* 25:8a. (Abstr.)

46. Neher, E., J. Sandblom, and G. Eisenman. 1978. Ionic selectivity, saturation, and block in gramicidin A channels. II. Saturation behavior of single channel conductances and evidence for the existence of multiple binding sites in the channel. *J. Membr. Biol.* 40:97–116.

47. Urban, B. W., S. B. Hladky, and D. A. Haydon. 1980. Ion movement in gramicidin pores. An example of single file transport. *Biochim. Biophys. Acta.* 602:331–354.

48. Heitz, F., N. Van Mau, R. Bennes, P. Daumas, and Y. Trudelle. 1989. Single channels and surface potential of linear gramicidins. *Biochimie.* 71:83–88.

49. Anderson, D. G., R. B. Shirts, T. A. Cross, and D. D. Busath. 2001. Noncontact dipole effects on channel permeation. V. Computed potentials for fluorinated gramicidin. *Biophys. J.* 81:1255–1264.

50. Bamberg, E., K. Noda, E. Gross, and P. Lauger. 1976. Single channel parameters of gramicidin A, B, and C. *Biochim. Biophys. Acta.* 419:223–228.

51. Jin, X.-Z. 1992. The impact of the negative charge on cation permeation in the taurine16 gramicidin A channel. Ph.D. thesis. Brown University, Providence, Rhode Island.

52. Hinton, J. F., J. Q. Fernandez, D. C. Shungu, and F. S. Millett. 1989. Thermodynamic parameters for the binding of divalent cations to gramicidin A incorporated into a lipid environment by Tl-205 nuclear magnetic resonance. *Biophys. J.* 55:327–330.

53. Woolf, T. B., and B. Roux. 1997. The binding site of sodium in the gramicidin A channel: comparison of molecular dynamics with solid-state NMR data. *Biophys. J.* 72:1930–1945.